Instantaneous flow-distribution measurements of the equilibrium turbulent region in a circular pipe using ultrafast NMR imaging

Katsumi Kose
Institute of Applied Physics, University of Tsukuba, Tsukuba 305, Japan
(Received 26 December 1990)

A powerful flow visualization and measurement method has been developed using ultrafast NMR imaging. This technique enables one to measure instantaneous distribution of any velocity component in any cross-sectional plane. This method was applied to the equilibrium turbulent region, or "puff," which is intermittently created by large disturbances in a circular pipe when the Reynolds number is around 2250. Instantaneous velocity component distributions were visualized and measured for two velocity components. The flow component parallel to the pipe axis clearly demonstrated the gross nature of the equilibrium puff and that perpendicular to the pipe axis visualized the detailed structures of vortices. Longitudinal vortices were clearly observed near the pipe wall at the upstream interface as well as around the pipe axis in the downstream region. The present measurements made for a single puff, in principle, agree with the ensemble-averaged results obtained in hot-wire measurements previously reported, both qualitatively and quantitatively.

I. INTRODUCTION

When large disturbances are introduced near the entrance of a pipe, turbulent flows are intermittently observed far downstream in the transitional region where the Reynolds number (Re) is between 2000 and 2700 [1,2]. These turbulent regions are known as "puffs" and observed to move indefinitely while preserving their lengths when the Re is around 2250 [2]. This stable puff is thus called the "equilibrium puff." Its self-sustenance mechanism is very interesting in itself as well as essentially important in understanding the lower critical Reynolds number of about 2000 observed in a circular pipe. However, there are only a limited number of studies dealing with this problem.

Extensive hot-wire measurements [1,2] were carried out by Wygnanski *et al.* and revealed fundamental characters of the equilibrium puff: turbulence is constantly produced near the upstream laminar to turbulent interface and its intensity decreases gradually towards the front of the puff. Thus the laminar to turbulent interface is clear in the upstream but not clear in the downstream of the puff. The ensemble-averaged results of the measurements presented a mean streamline of the equilibrium puff. They thus suggested the presence of a large toroidal vortex near the upstream interface.

A flow visualization experiment of the equilibrium puff was reported by Bandyopadhyay in 1986 [3]. He observed various organized motions: high-speed laminar plug flows around the pipe axis flowing into the turbulent region near the upstream interface, shedding of a train of wakelike vortices and helical motions near the upstream interface, and longitudinal vortices in the downstream region. He thus concluded that the large toroidal vortex is not present near the upstream interface.

The first nuclear magnetic resonance (NMR) experiment of the puff was carried out by Fukuda *et al.* in 1985 [4]. They observed an asymmetric turbulent intensity distribution in the puff along the pipe axis and measured the intermittency factor in the transitional region. Their experiment, however, had no spatial resolution in the direction perpendicular to the pipe axis. Quite recently, visualization of the equilibrium puff using ultrafast NMR imaging was reported by the present author [5]. This work succeeded in a quantitative evaluation of the vortex motions as well as clear visualization of the vortex structures and distributions in a cross-sectional plane perpendicular to the pipe axis. The present paper is a comprehensive extension of the previous brief communication [5] and has two purposes: The first is to develop a method for instantaneous flow distribution measurements using ultrafast NMR imaging. The second is to clarify the detailed turbulent structure of the equilibrium puff using the developed method.

Conventional NMR imaging techniques now widely used in medical imaging systems require at least several seconds to take a two-dimensional cross-sectional image. These techniques thus cannot be applied to studies of essentially unsteady phenomena such as turbulence. Ultrafast NMR imaging [6–9] pioneered by Mansfield *et al.* realizing a very short data acquisition time (several tens of milliseconds) is thus indispensable for studies of turbulence. The present author has reported the first study of turbulence using this technique and demonstrated that this method is a powerful tool in visualizing organized fluid motions [5].

Ultrafast NMR imaging has three outstanding advantages in flow measurements [5,9,10]. First, it can measure selectively any velocity component at many (1000–10 000) positions at the same time. This property facilitates detection of various organized fluid motions. Second, no disturbance is introduced during the flow measurement. Although the object fluid must be placed in a relatively strong static magnetic field and exposed to

temporally changing magnetic-field gradients and radio-frequency magnetic fields, no detectable change of flow is conceivable so long as the fluid is nonconductive and nonmagnetic. Third, any cross-sectional plane can be visualized. This property enables observations in planes which could otherwise never be accessed with other methods.

There are, of course, several disadvantages in ultrafast NMR imaging. The first is that object fluids must be liquids containing sufficient amounts of NMR sensitive nuclei. The second is the low in-plane resolution (128×128 pixels at most) and the relatively long measurement time (10–100 msec). The third is that the obtained image is very sensitive to magnetic-field inhomogeneities in the object. These field inhomogeneities originate from heterogeneous distribution of the liquid and surrounding materials as well as the applied magnetic field [11].

This paper consists of five major sections. In Sec. II a flow measurement method using ultrafast NMR imaging and a computer simulation for vortex visualization is presented. In Sec. III experimental apparatus and procedures are described. The obtained NMR images and related results are presented in Sec. IV and summarized in Sec. V.

II. METHOD AND COMPUTER SIMULATION

A. A method for instantaneous flow distribution measurement

The approaches to NMR flow measurements can be divided into two categories: the amplitude method [12–14] and the phase method [15–19]. These terms come from the fact that amplitude or phase of nuclear spin magnetization is utilized in detecting flow velocity. In this section, flow measurement techniques using the phase method in ultrafast NMR imaging are described [5,9,10].

All the NMR imaging techniques presently used employ a two- or three-dimensional frequency spectrum to resolve the spatial positions of nuclear spins. In other words, a nuclear magnetization at a spatial position corresponds to a multidimensional frequency component due to applications of magnetic-field gradients fixed in the spatial coordinates. Thus spin motions produce various phenomena as described below.

The first consequence of spin motion is blurring of the spatial position of spins as naturally expected. However, the most important or useful phenomenon is the phase shift observed in the NMR image, which corresponds to the phase deviation of the nuclear precession at each position. This effect is caused by the fact that nuclear spins move under the application of magnetic-field gradients, that is, the precession frequency of the nuclei changes while they move. In most flow applications, the phase shifts are measured under the condition in which the blurring effect can be neglected and used for the flow distribution measurement [20,21].

Figure 1 schematically shows a cross-sectional plane imaged with an ultrafast NMR imaging pulse sequence. When nuclear spins at a position (y,z) in the plane have

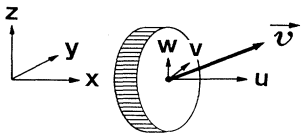

FIG. 1. A cross-sectional plane imaged with ultrafast NMR imaging. These spatial coordinates are in accordance with the experimental arrangement described in Sec. II.

instantaneous velocity components u, v, and w, then the phase shift $\phi(y,z)$ of the nuclear magnetization is expressed in good approximation as

$$\phi(y,z)=\alpha u(y,z)+\beta v(y,z)+\gamma w(y,z) , \tag{1}$$

where α, β, and γ are constants determined by the waveforms of the magnetic-field gradients used in the pulse sequence [5,10]. This equation shows that the phase shift is proportional to the velocity component parallel to the vector $(\alpha,\beta,\gamma,)$. In other words, the velocity component projected onto the vector determined in the sequence is observed through the NMR images.

Since the constants α, β, and γ can take any values if the waveforms of the field gradients are properly designed, any velocity component can be selectively visualized. For example, when α is nonzero and β and γ are made zero, the distribution of u is visualized or measured. Nearly simultaneous measurement of two or three velocity components is also possible if images with different velocity component sensitivity are successively measured in a very short time using such a technique as a multiple spin-echo sequence. This technique enables a visualization of instantaneous flow vectors in a cross-sectional plane [10].

Two kinds of NMR images are obtained through the mathematical image reconstruction process, that is, the two-dimensional Fourier transform of the acquired signal. These images are called real and imaginary images and their intensities $R(y,z)$ and $I(y,z)$ are expressed as

$$R(y,z)=k\rho(y,z)\cos\phi(y,z) , \tag{2}$$

$$I(y,z)=k\rho(y,z)\sin\phi(y,z) , \tag{3}$$

where k is a constant and $\rho(y,z)$ is the nuclear spin density in the cross-sectional plane. The effects of nuclear relaxation times on the intensities are neglected. Since the phase shift $\phi(y,z)$ is proportional to a flow component as described above, these images reflect the flow distribution through the nonlinear functions to cosine and sine. These images are, however, very useful to detect organized motions as reported previously [5] because no post-processing of the images is required.

The phase distribution $\phi(y,z)$ can be calculated from the arctangent of the ratio of the imaginary to the real-image value at each pixel. This calculation, however, often accompanies some difficulties due to two phenome-

na described below. The first is the effect of velocity gradient: when there is a large velocity gradient across a pixel, the nuclear magnetizations in the pixel cancel each other thus producing little intensity on the pixel. This effect is often serious in two-dimensional NMR images because the slice thickness is usually several times as large as the transverse pixel dimension. The second is the aliasing of the phase angle when the phase shift exceeds $\pm\pi$ values. Although flow visualization using the real or imaginary images is relatively free from these effects, quantitative velocity distribution measurements using the phase shift must be carried out under conditions in which these effects do not produce any serious errors.

B. Computer simulation for vortex motions

In this section, some patterns which will be experimentally presented in Sec. IV are mathematically simulated. Figure 2 shows a model of a vortex and a cross-sectional plane: an axisymmetric vortex of which rotation axis makes a polar angle θ with the x axis and an azimuthal angle φ with the y axis is imaged in the cross-sectional plane. Velocity components u,v, and w of a fluid particle located in a position (y,z) in the plane are expressed as follows:

$$\begin{aligned} u &= V\sin\delta\sin\theta \ , \\ v &= -V\sin\delta\cos\theta\cos\varphi - V\cos\delta\sin\varphi \ , \\ w &= -V\sin\delta\cos\theta\sin\varphi + V\cos\delta\cos\varphi \ , \end{aligned} \tag{4}$$

where

$$\begin{aligned} \cos\delta &= Y\cos\theta/(Y^2\cos^2\theta+Z^2)^{1/2} \ , \\ \sin\delta &= Z/(Y^2\cos^2\theta+Z^2)^{1/2} \ , \\ V &= V_0[1-\exp(-br^2)]/r \ , \end{aligned} \tag{5}$$

and

$$\begin{aligned} Y &= y\cos\varphi + z\sin\varphi \ , \\ Z &= -y\sin\varphi + z\cos\varphi \ , \\ r &= (Y^2\cos^2\theta+Z^2)^{1/2} \ . \end{aligned} \tag{6}$$

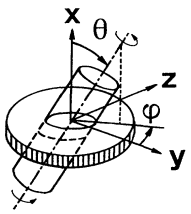

FIG. 2. A model of a vortex and a cross-sectional imaging plane used in the computer simulation.

In these equations, V_0 and b are constants which characterize the vortex motion. The velocity distribution in the vortex is assumed to be that of Oseen's two-dimensional vortex. The derivation of Eq.(4) will be given in the Appendix.

When the phase shift ϕ of nuclear spins is represented by $\phi=\beta v$, that is, when the velocity component along the y axis is visualized, the intensity of the real and imaginary part of the image can be expressed as

$$R(y,z)=k\rho(y,z)\cos\beta v \ , \tag{7}$$

$$I(y,z)=k\rho(y,z)\sin\beta v \ . \tag{8}$$

Figure 3 shows calculated results of $R(y,z)$ [(a) and (c)] and $I(y,z)$ [(b) and (d)] for various vortex orientations; the values shown below the images represent the pair of angles (θ,φ).

Each image in Fig. 3 consists of 128×128 pixels and the axis of the vortex is placed at the center of the image. The constant b gives the position where the fluid speed reaches a maximum and the product of β and V_0 determines the maximum value of the phase shift. In the computer simulation, the constant b is selected in such a way that the maximum speed is realized at the positions about

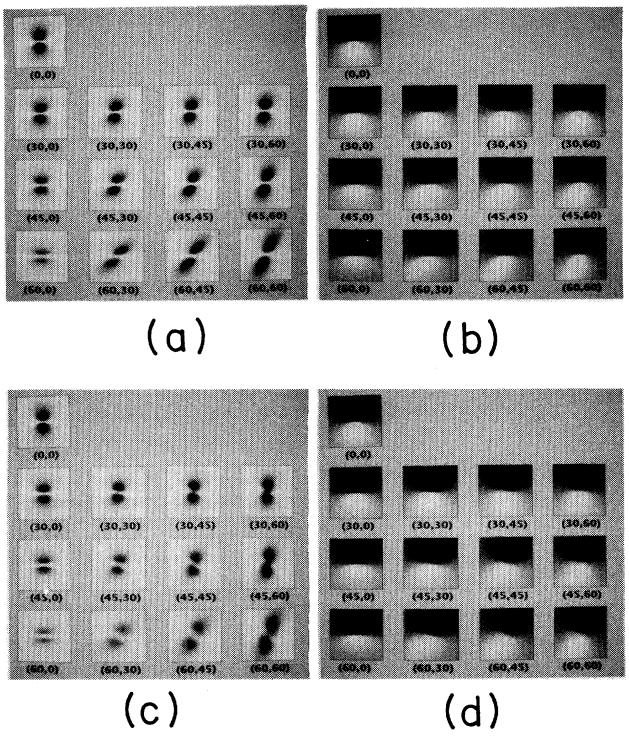

FIG. 3. Calculated images of the model vortex. The pair of numbers displayed below the images are the angles (θ,φ). (a) and (c) are real part images and (b) and (d) are imaginary part images. Slice thickness is zero in (a) and (b) and about twice as large as the diameter of the vortex core in (c) and (d).

9 pixels apart from the center of the image when the vortex axis is perpendicular to the cross-sectional plane. The maximum phase shift value is determined to be 2.7 rad in these calculations.

In Figs. 3(a) and 3(b), the thickness of the cross-sectional plane is assumed to be zero. On the other hand, in Figs. 3(c) and 3(d), the slice thickness is assumed to be 36 pixel length. This length is about twice as large as the diameter of the vortex core which is the region surrounded by the surface with the maximum axial velocity. All the real and imaginary part images show pairs of dark spots and pairs of a dark spot and a bright spot aligned nearly parallel to the z direction regardless of the angles θ and φ. From the symmetry consideration, it is noted that these images can cover a considerable fraction of all the vortex orientations. Thus a vortex of this kind will be often visualized like the pair of spots as described above if it is sliced by the imaging plane. When the angle θ is small, the vortex can be considered a longitudinal vortex because the vortex axis is nearly parallel to the main flow. Though other vortex configurations or other kinds of vortex are, of course, conceivable, this model is often realized in the present experiment as we will see in the images presented in Sec. IV.

III. EXPERIMENT

A. Apparatus

Steady water flow in a horizontal polycarbonate pipe was produced using a constant head tank system. The inner diameter D and the total length of the pipe was 18 and 3600 mm ($=200D$), respectively. A plate with a 10-mm orifice was placed near the inlet of the pipe to introduce large disturbances into the flow. The longitudinal relaxation time of the water protons was adjusted to be about 60 ms by dissolving $CuSO_4$ crystals in the test liquid. The water was recirculated using a constant current pump and the flow rate was controlled with a bulb near the outlet of the pipe. The temperature of the water was kept within $28\,^{\circ}C \pm 0.2\,^{\circ}C$ throughout the experiment to reproduce the Reynolds number of the flow. Cross-sectional planes (4-mm thick) perpendicular to the pipe axis were imaged at downstream positions $x = 10D$, $20D$, $30D$, $40D$, $50D$, $60D$, $120D$, and $180D$, where x was the distance from the orifice. Equilibrium puffs were imaged at $x = 120D$ or $180D$.

NMR images were taken with a home-built NMR imaging system utilizing an iron-core electromagnet. The diameter of the pole pieces and the air-gap of the magnet were 300 and 66 mm, respectively. The operating field strength was 1.0 T, that is, the resonance frequency of the protons was about 42.6 MHz. Three pairs of magnetic-field gradient coils were wound on a pair of Bakelite plates and attached to the pole faces of the magnet. The coils were driven by three constant current bipolar power amplifiers whose maximum output current was 10 A. The gradient field strengths per unit current were about 0.7, 1.1, and 0.7 G/cm for the G_x, G_y, and G_z coils, respectively. The Cartesian coordinates were defined to agree with those of the flow system as described in Fig. 1: the x axis was the horizontal direction perpendicular to the magnetic field, the y axis was the horizontal direction parallel to the field, and the z axis was the vertical direction.

A solenoid coil with a diameter 28 mm and a length of about 30 mm was used as both the transmitter and receiver coil. The coil was fixed in a rf shield box made of 0.3-mm thick brass plates in order to decrease eddy currents generated in the plates as well as to eliminate rf external noise. The rise time (from 0 to 95 % of the final value) of the field gradients was thus about 100 μs.

NMR pulse sequences were generated using a flexible pulse generator utilizing a microprocessor chip (Z80H). The sampled NMR data were processed with a 32-bit microprocessor (MC68020) based computer system to form NMR images.

B. Pulse sequence and data processing

Figure 4 shows the pulse sequence used in the present study. The spin-echo time which corresponds to the difference between the 90° pulse and the peak of the spin echo was chosen to be 24 ms or 28 ms. The length of one-cycle of the oscillating gradient (G_y) was 1.28 ms, thus the total date-acquisition time for one image was 20.48 ms (16 cycles). The intensity of the read-out gradient was 9.8 G/cm. The duration time of the blipped phase encode gradient (G_z) was 0.2 ms.

This pulse sequence was repeated continuously at 200 ms time intervals and the NMR signal was observed on an oscilloscope as well as successively sampled and stored in the computer memory. Since the passage of a puff was easily identified by a drastic change in the signal, the data acquisition was interrupted manually after the passage of a puff.

Two-channel NMR signals were digitized continuously

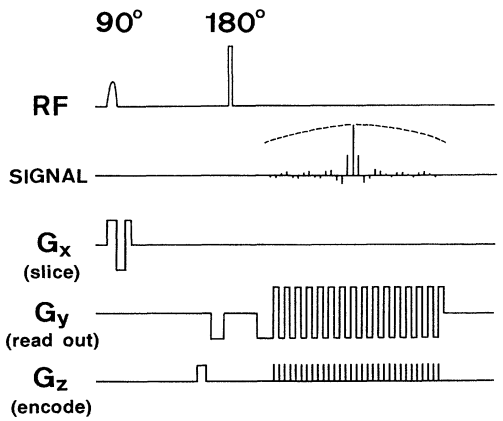

FIG. 4. Pulse sequence used in this study. The lines show timing charts of the rf pulse sequence, NMR signal, and three magnetic-field gradients.

at the 10-μs sampling rate. Thus 4096 data points (2048 points per channel) were available for one image. However, only separate 32 sets of 64 data points (1024 points per channel) sampled while the oscillating read-out gradient G_y was nearly constant were used for the image reconstruction of a 32×32 pixel image. The field of view and the pixel size was 24×24 mm^2 and 0.75×0.75 mm^2, respectively. Since phase shifts caused by eddy currents due to the read-out gradient switching produced large phase errors in the NMR signal, the errors were corrected before the image reconstruction using phase values measured without the phase encode gradient G_z.

IV. RESULTS AND DISCUSSION

A. Flow parallel to the pipe axis

Figure 5 shows two image series of equilibrium puffs visualized with the flow parallel to the pipe axis when the Reynolds number was 2250. The images were consecutively taken at 200-ms time intervals and 36 of them are displayed from the upper left to the lower right. These images show only the real part, thus proton densities multiplied by cosine of the velocity component u are displayed. The ghost pattern, the center of which is near the edge of each image, is an artifact produced by mismatching between the data sampled under the positive read-out gradient and those sampled under the negative read-out gradient. Though artifacts of this kind will also be seen in the images shown later, it does not interfere with understanding the flow distribution because their nature is well known.

It should be noted that a single bright or dark area represents a region with nearly the same velocity. As a result, the laminar flow is visualized as a pattern of several coaxial rings as seen in the first and the last images of Fig. 5(a). The turbulent regions in the equilibrium puff are visualized with disturbed patterns seen in the fourth and fifth rows of Figs. 5(a) and 5(b).

The coefficient α described in Sec. II which relates the phase shift to the velocity component is 1.0 and 0.5 rad/(cm/s) in Figs. 5(a) and 5(b), respectively. Since the central bright spots of the laminar flow images in Fig. 5(a) represent about 6π radian phase shift, the flow speed is about 20 cm/sec. This value agrees with the mean flow velocity of about 10.5 cm/sec.

We can clearly see several characteristic flow distributions in these images. The most prominent pattern is the fast laminar plug flow around the pipe axis near the upstream interface flowing into the turbulent region, which is most clearly displayed in (5,6), (6,1), and (6,2) images in Fig. 5(a), where (n,m) represents the position of the nth row and the mth column in the figure. The next interesting flow pattern is the nearly flat velocity distribution around the pipe axis observed in the downstream region of the puff, which is seen in the second and the third rows in Fig. 5(a) as central large dark regions.

These two characteristic flow patterns are also visualized in Fig. 5(b), although this figure is less sensitive than Fig. 5(a). Figure 5(b) is, however, more suitable for phase

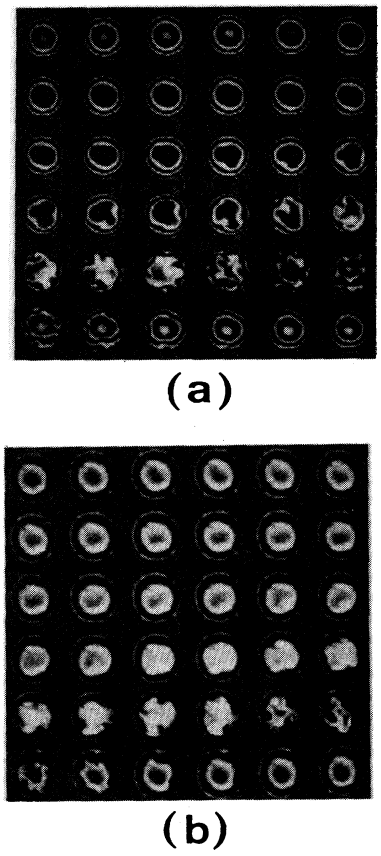

FIG. 5. Cross-sectional NMR images of equilibrium puffs visualized with the flow parallel to the pipe axis. Reynolds number is 2250. The coefficient α is 1.0 and 0.5 rad/(cm/s) in (a) and (b), respectively. 36 consecutive images taken at 200-ms time intervals are displayed from the upper left to the lower right. Only real part images are displayed.

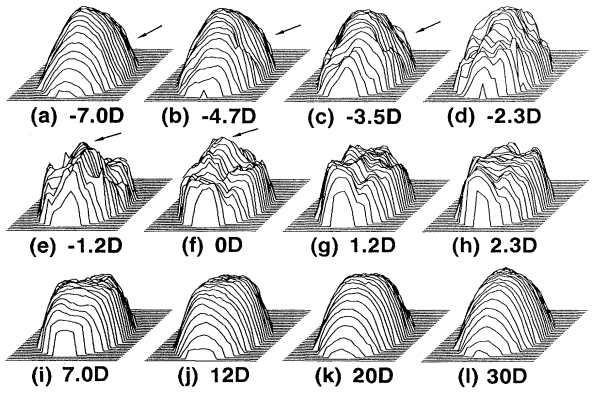

FIG. 6. Instantaneous distributions of the flow component along the pipe axis in the equilibrium puff. The captions displayed under the figures are the distances from the upstream interface at the pipe axis. Poiseuille flow is realized near the upstream and far downstream from the upstream laminar to turbulent interface.

calculation because phase dispersion in a pixel and aliasing of phase angle are not so serious as in Fig. 5(a). Phase images can be thus calculated using Fig. 5(b) and the corresponding imaginary images as described in Sec. II. Typical phase distributions are displayed in Fig. 6. These figures show instantaneous velocity distributions along the pipe axis, of which measurement time is about 20 msec. The captions shown below the figures represent distances from the upstream laminar to turbulent interface where the front of the laminar plug flow contacts the turbulent region near the pipe axis. This laminar plug is clearly seen and indicated by the arrows in Figs. 6(e) and 6(f).

Figure 6 most clearly shows several fundamental properties of the equilibrium puff: The first is that just upstream of the laminar to turbulent interface, the flow is highly turbulent and the velocity distribution is nearly constant except near the pipe wall [Figs. 6(g) and 6(h)]. The second is that the nearly velocity constant area around the pipe axis corresponding to the turbulent region decreases gradually towards the front of the puff [Figs. 6(i)–6(k)]. However, even where the distance from the upstream interface is 20 times the pipe diameter, the profile does not appear parabolic. Fully developed Poiseuille flow is established far downstream from the upstream interface as seen in Fig. 6(l). The third property is that the Poiseuille flow is nearly established just upstream of the laminar to turbulent interface except near the pipe wall [Figs. 6(a)–6(c)]. The turbulence near the wall appears to have a structure stretched along the pipe axis, which is indicated by the arrows in Figs. 6(a)–6(c).

Figure 7 shows mean flow speed variations in the equilibrium puff plotted against the distance from the upstream interface, which is calculated with the flow distribution shown in Fig. 6. The black and the white circles represent the speed averaged in the central and the outer regions displayed in the figure. This figure resembles the results obtained with the hot-wire measurements [2] and clearly shows that the mean velocity decreases rapidly near the interface and gradually recovers to that of the laminar flow when the distance x increases from $-10D$ to $40D$. One interesting observation is that the two regions have nearly the same mean velocity in the highly turbulent region just downstream of the upstream interface.

Though results presented in this section are identical to those of hot-wire measurements [2] and flow visualization [3], it must be remarked that these measurements are performed for a single puff and no statistical treatment has been carried out. In addition, it should be emphasized that the instantaneous velocity distributions in a puff have been measured with this method and the measurement time for them is less than 10 sec.

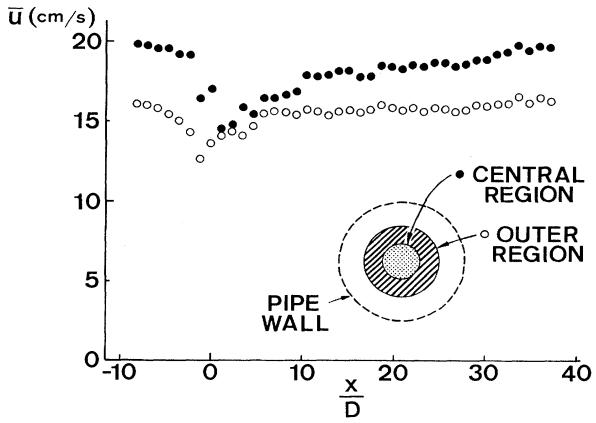

FIG. 7. Variation of mean flow velocities along the pipe axis in the equilibrium puff. Black and white circles show mean velocities in the central and the outer region described in the figure. Near the upstream interface, these two circles show similar values, representing the presence of strong turbulent mixing in the cross-sectional plane.

B. Flow perpendicular to the pipe axis

Figure 8 shows three image series visualized with the flow perpendicular to the pipe axis when the Reynolds number is of 2000 [(a)] and 2250 [(b) and (c)]. These images were consecutively taken at 200-ms time intervals and 16 of them are displayed from the upper left to the lower right. These images show the real part, thus proton densities multiplied by the cosine of the velocity component v are displayed. No intensity variation is observed in the laminar flow images in Fig. 8(a) because the flow is always parallel to the pipe axis. On the other hand, in Figs. 8(b) and 8(c) equilibrium puffs are clearly visualized with the flow component normal to the pipe axis as dark and bright patterns.

The coefficient β described in Sec. II which relates the phase shift to the velocity component v is 4.5 rad/(cm/s). Thus dark areas seen in these images correspond to regions where the phase shift exceeds about $\pm\pi/2$ rad, that is, the absolute value of the flow component v is larger than about 0.3 cm/s. Most bright areas, on the other

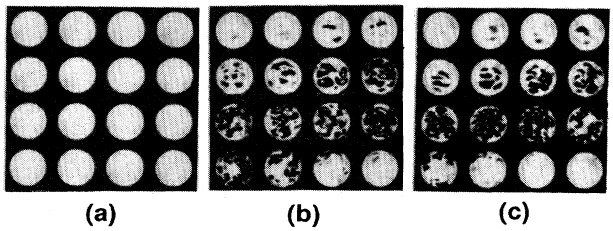

FIG. 8. Cross-sectional NMR images visualized with the flow perpendicular to the pipe axis. (a) Reynolds number is 2000. The flow is laminar and there is no flow component perpendicular to the pipe axis. (b) and (c) Reynolds number is 2250. An equilibrium puff is visualized with the flow component perpendicular to the pipe axis. 16 consecutive images are displayed from the upper left to the lower right. Only real part images are displayed.

hand, correspond to regions where $|v|$ is less than 0.3 cm/s. There are, of course, bright regions where the phase shift exceeds about $\pm 3\pi/2$, that is, $|v|$ is larger than about 1.0 cm/sec. Since such bright regions must be surrounded by dark regions, it is straightforward to distinguish turbulent regions from laminar regions in the images shown in Fig. 8.

The distribution of turbulence in the equilibrium puff thus nearly corresponds to that of dark regions, which increase their area and decrease their size from downstream to upstream, that is, the upper left to the lower right in Figs. 8(b) and 8(c). The total area of the dark spots reaches a maximum near the upstream interface and a bright laminar region near the pipe axis appears at the interface. This laminar region visualized in the 12th image of Fig. 8(b) and the 13th image of Fig. 8(c) is the same one as the laminar plug flow observed in Figs. 5 and 6. Further upstream, turbulent regions still exist near the pipe wall as seen in the 13th and 14th images of Fig. 8(b) and 14th and 15th images of Fig. 8(c).

Most dark spots are considered to be various vortices as described in the computer simulation presented in Sec. II. Several typical images are displayed in Fig. 9. Figures 9(a) and 9(b) are longitudinal vortices observed in the downstream region, which have been reported also in flow visualization [3] and the short communication of this study [5]. In Fig. 9(a), the real part image visualizes two vortices and the imaginary part shows that they are rotating in the same direction because the pairs of dark and bright spots have the same order along the z direction. The imaginary part, however, visualizes a few vortices in addition to the vortices displayed in the real image. In Fig. 9(b), the real part image detects two clear and two less clear vortices and the imaginary part image shows that the two clear vortices are rotating in the reverse direction to each other because the pairs of the dark and bright spots have an opposite order along the z direction.

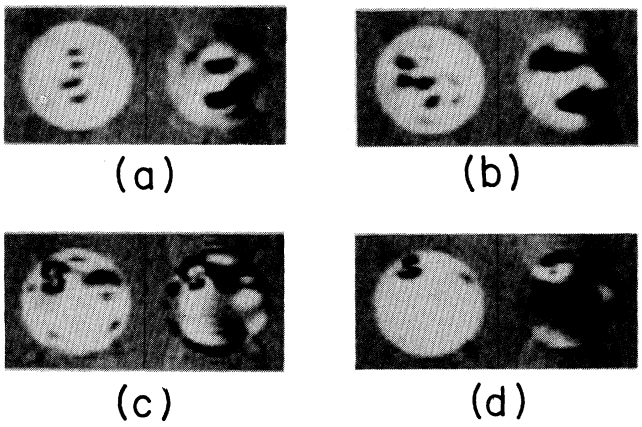

FIG. 9. Longitudinal vortices observed in the downstream region [(a) and (b)] and at the upstream interface [(c) and (d)]. The left and right images show real and imaginary images, respectively. (c) and (d) are consecutive images taken in an equilibrium puff.

Figures 9(c) and 9(d) are longitudinal vortices observed at the upstream interface. In both the images, typical longitudinal vortex patterns are visualized near the top of the water images. These images are, in fact, two successively acquired images whose spatial separation along the pipe axis is about $1.2D$ (20 mm). Thus these patterns most probably correspond to a single large longitudinal vortex. Although these longitudinal vortices are usually seen at the upstream interface of the equilibrium puff, the generation mechanism is unknown. The presence of these vortices may provide the reason why the upstream interface is not clear near the pipe wall as observed in hot-wire measurement [2].

Figure 10 shows real, imaginary, and calculated phase images of the equilibrium puff. The measurement condition is identical to that in Fig. 8 except that the coefficient β is 1.1 rad/(cm/s); this value is about a quarter of that in Fig. 8. Figure 10(c) thus shows the distribution of the velocity component v in grey scale. Typical patterns of vortices are seen in the velocity distribution. It is noted that even in the highly turbulent region just downstream of the upstream interface, large scale patterns are observed. This result indicates that though the real and imaginary images represent the averaged intensities over the slice and the calculated phase has also some averaged character, large scale motions are present in the highly turbulent region.

Figure 11 shows means of v^2 calculated from phase images of three puffs plotted against the distance from the upstream interface. The mean is calculated in the central circular area whose diameter is $1/\sqrt{2}$ the pipe diameter. The solid curve shows the result evaluated from hot-wire measurements [2]. Though the present data points scatter above the curve, the quantitative agreement is good. Thus this figure demonstrates that the flow component perpendicular to the pipe axis is accurately detected.

To summarize the above results, distributions, and structures of vortices or turbulence in the equilibrium puff are clearly visualized with the velocity component perpendicular to the main flow. The observed distribution of turbulence is in good accord with that obtained with the main flow component as well as that obtained

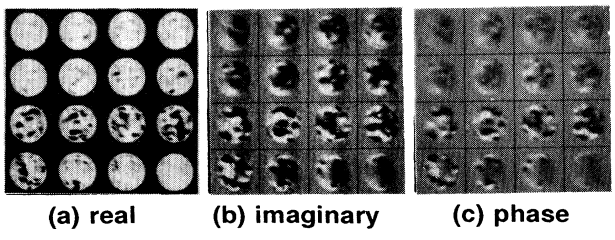

FIG. 10. (a) Real, (b) imaginary, and (c) phase images of an equilibrium puff visualized with the flow perpendicular to the pipe axis. These images are taken consecutively at 200-ms time intervals and displayed from the upper left to the lower right. The phase image directly shows distribution of the velocity component v.

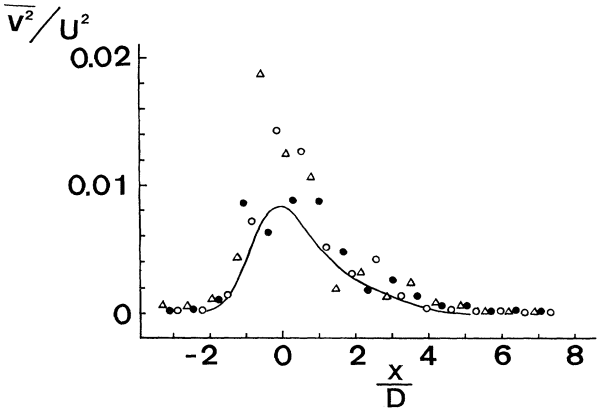

FIG. 11. Means of v^2 calculated in the cross-sectional plane plotted against the distance from the upstream interface. The calculation is carried out for the central circular area whose diameter is $1/\sqrt{2}$ the pipe diameter. Results for three puffs are displayed with white circles, black circles, and white triangles. The solid line shows the result evaluated from hot-wire measurements [2].

with hot-wire measurements [2]. The threshold value of about 0.3 cm/s for the detection of turbulence is only 3% of the mean main flow speed (10.5 cm/s). Thus this fact shows that this visualization technique is very sensitive in detecting turbulent structures in a relatively fast main flow.

C. Model of the equilibrium puff

The flow visualization experiment [3] divided the equilibrium puff into three sections from the upstream to the downstream: The first section is the upstream interface region where a clear laminar to turbulent interface, a laminar plug flow near the pipe axis, helical motions, and vortex shedding processes are observed. The second section is the fully turbulent region just downstream of the first section. The third section is the relaminarizing region where longitudinal vortices and other vortices are decaying gradually towards the front of the puff.

Though the present experiment supports this classification, in principle, some additional results from this study can be added to the model. The additional results are longitudinal vortices near the pipe wall at the upstream interface, large scale turbulent structures in the fully turbulent region, and the very long (about 20D) relaminarizing region. Though the length of the relaminarizing region is reported to depend on the Reynolds number and the downstream interface is not clear, this study has clearly demonstrated the presence of turbulence near the pipe axis far downstream of the puff as seen in Fig. 6(k). An improved model of the equilibrium puff obtained in this study is shown in Fig. 12. The boundary between the highly turbulent and the relaminarizing region is not definite, however, the classification is useful because most turbulent energy is present in the highly turbulent region as seen in Fig. 11.

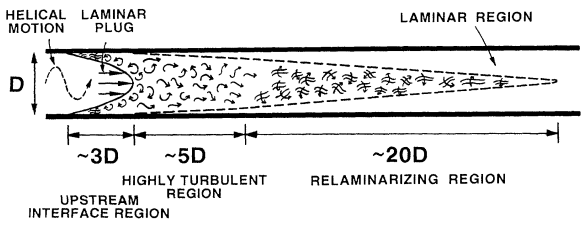

FIG. 12. A model of the equilibrium puff derived from the present experiment and flow visualization [3].

D. Process of puff formation

The images of equilibrium puffs presented in the preceding sections are observed at the position $x = 120D$ or 180D downstream from the orifice as mentioned before. At these positions, the typical turbulent structures of the equilibrium puff are visualized as Figs. 5 and 8. At the positions closer to the orifice, however, the characteristic pattern of the puff is not seen. Figure 13 shows six image series consecutively obtained at the positions $x = 10D$ [(a)], 20D [(b)], 30D [(c)], 40D [(d)], 50D [(e)], and 60D [(f)]. The measurement condition is identical with that in Fig. 8. In these cross sections, a number of typical vortex or swirling patterns are visualized.

At $x = 10D$, the cross section is filled with a large number of small vortices which must be created just downstream of the orifice. At $x = 20D$, however, the size of the vortices appears to increase and the total area of the

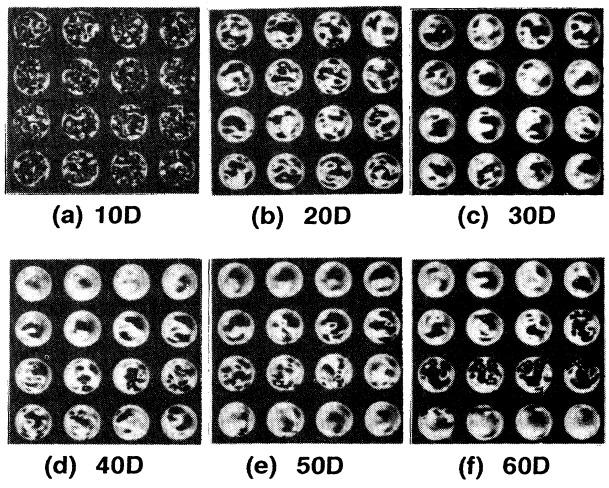

FIG. 13. Images taken at (a) $x = 10D$, (b) 20D, (c) 30D, (d) 40D, (e) 50D, and (f) 60D. Real part images taken at 200-msec time intervals are displayed from the upper left to the lower right. These images show that the turbulence produced near the orifice gradually decay as the flow goes downstream ($x = 10D-30D$), however, inhomogeneous turbulent distributions along the flow direction are observed at more downstream positions ($x = 40D-60D$).

dark regions appears to decrease compared with those at $x=10D$. The same tendency is seen also at $x=30D$. In these regions ($x=10D-30D$), the size and the total area of the dark spots appear to be roughly constant throughout the single image series. These results thus indicate that the vortices made near the orifice are combined together as the flow goes downstream.

At $x=40D$, however, the distribution and the size of dark spots becomes inhomogeneous along the pipe axis as seen in Fig. 13(c). This phenomenon is more clearly observed at $x=50D$ and $60D$. The high density distribution of vortices along the flow direction seen in Fig. 13(f) is thus considered to be an "embryo" of the equilibrium puff. The pattern of this piece of turbulence is similar to that of the equilibrium puff. Thus one can say that the image series in Fig. 13 visualize the formation process of the equilibrium puff.

Hot-wire measurements [1] have reported the nature of turbulence near obstructions (orifice, disk, etc.) in a circular pipe. They observed high-level turbulence at $x=15D$ and relatively homogeneous turbulent flows where x is less that $30D$. Further downstream, they also observed intermittent turbulent flows. This fact agrees well with the NMR images shown in Fig. 13.

V. CONCLUDING REMARKS

In the present study, the equilibrium puff was visualized with two velocity components: the velocity component parallel to the pipe axis clearly visualized the gross nature of the puff and that perpendicular to the pipe axis visualized detailed structures of the organized motions. The ultrafast NMR imaging technique presented in this study has also enabled measurements of the instantaneous flow distributions in the equilibrium puff. Though the results obtained agree with hot-wire measurements and flow visualization experiment previously reported, a number of organized motions such as longitudinal vortices have been more clearly visualized.

Ultrafast NMR imaging can provide quantitative fluid velocities as well as patterns of various organized fluid motions. The quantitative data were, however, rather scattered compared with those of hot-wire measurements because of the low sensitivity of NMR itself. This technique, however, has a unique advantage over other flow visualization methods because the visualized pattern always includes quantitative information and any flow component is visualized in any plane. This property is more suitable for detection of organized motions in turbulence than for quantification of turbulence. However, since hot-wire measurements are often very time consuming when some volume must be scanned, in such case ultrafast NMR imaging can be a very powerful experimental tool and give a guide for further precise measurements.

In order to understand the self-sustenance mechanism of the equilibrium puff, more experimental research is required. The author thinks that NMR measurements of the equilibrium puff at various Reynolds numbers in the transitional region ($2000<\mathrm{Re}<2700$) will give very valuable information about the sustenance mechanism. The ultrafast NMR imaging technique will then be an indispensable tool because this technique gives sufficient information in a very short time.

ACKNOWLEDGMENTS

The author thanks Professor T. Inouye for continuing encouragement throughout this work and Dr. S. Matsui for valuable discussions. He also thanks Professor S. Tsugé and Professor K. Matsuuchi for helpful suggestions and Dr. Paul Fons for a critical reading of this manuscript. This work was supported in part by Grants-in-Aid for Scientific Research from the Ministry of Education, Science and Culture in Japan.

APPENDIX: VELOCITY COMPONENTS OF A CIRCULAR VORTEX IN A CROSS-SECTIONAL PLANE

In this appendix, velocity components of the fluid in the cross-sectional plane described in Fig. 2 is derived. Figure 14 shows the configuration of the model vortex and the cross-sectional plane used in the computer simulation in Sec. II. It is assumed that the model vortex is axisymmetric and its axis makes a polar angle θ with the x axis and an azimuthal angle φ with the y axis. The radial velocity $V(r)$ in the vortex is taken as

$$V(r)=V_0[1-\exp(-br^2)]/r\ , \tag{A1}$$

where V_0 and b are constants and r is the distance from the central axis of the vortex.

Let us calculate the velocity components u,v, and w at the position $P(0,y,z)$ in the cross section (yz plane). The ellipse passing P shown in Fig. 14(a) represents the cross section of the model vortex in which the fluid has the same radial velocity around the axis of the vortex. By a $-\varphi$ rotation around the x axis, this ellipse is transformed to another ellipse whose principal axes are parallel to the y and z directions, respectively. The position P is also transformed to the position $Q(0,Y,Z)$ on the latter ellipse. By a $-\theta$ rotation around the z axis, the axis of the model vortex becomes parallel to the x axis and the position Q is transformed to the position $R(Y\sin\theta, Y\cos\theta, Z)$.

The velocity components $u(R)$, $v(R)$, and $w(R)$ at the

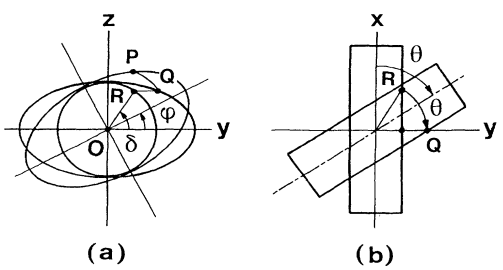

FIG. 14. Configuration of a model vortex in a cross-sectional plane. The ellipses show cross sections of the vortex where the radial speed is constant.

position R are expressed as

$$u(R)=0\ ,$$
$$v(R)=-V(r)\sin\delta\ , \tag{A2}$$
$$w(R)=V(r)\cos\delta\ ,$$

where r is the distance between the central axis of the vortex and the position R, that is,

$$r^2=(Y\cos\theta)^2+Z^2\ , \tag{A3}$$

and δ is the angle between OR and the y axis in the yz plane. Thus $\cos\delta$ and $\sin\delta$ are expressed as

$$\cos\delta=Y\cos\theta/(Y^2\cos^2\theta+Z^2)^{1/2}\ , \tag{A4}$$
$$\sin\delta=Z/(Y^2\cos^2\theta+Z^2)^{1/2}\ . \tag{A5}$$

The velocity components $u(Q)$, $v(Q)$, and $w(Q)$ at the position Q are thus calculated by a θ rotation around the z axis as

$$u(Q)=V(r)\sin\delta\sin\theta\ ,$$
$$v(Q)=-V(r)\sin\delta\cos\theta\ , \tag{A6}$$
$$w(Q)=V(r)\cos\delta\ .$$

Since the velocity components $u(P)$, $v(P)$, and $w(P)$ at the position P are expressed as

$$u(P)=u(Q)\ ,$$
$$v(P)=v(Q)\cos\varphi-w(Q)\sin\varphi\ , \tag{A7}$$
$$w(P)=v(Q)\sin\varphi+w(Q)\cos\varphi\ ,$$

we can calculate them by substituting Eq. (A6) in Eq. (A7) and using the relation,

$$Y=y\cos\varphi+z\sin\varphi\ , \tag{A8}$$

$$Z=-y\sin\varphi+z\cos\varphi\ . \tag{A9}$$

The final form for the velocity components u,v, and w at the position P is thus written as

$$u=V(r)\sin\delta\sin\theta\ ,$$
$$v=-V(r)\sin\delta\cos\theta\cos\varphi-V(r)\cos\delta\sin\varphi\ , \tag{A10}$$
$$w=-V(r)\sin\delta\cos\theta\sin\varphi+V(r)\cos\delta\cos\varphi\ ,$$

where $V(r)$, r, $\cos\delta$, and $\sin\delta$ are given in Eqs. (A1), (A3), (A4), and (A5).

[1] I. J. Wygnanski and F. H. Champagne, J. Fluid Mech. **59**, 281 (1973).
[2] I. J. Wygnanski, M. Sokolov, and D. Friedman, J. Fluid Mech. **69**, 283 (1975).
[3] P. R. Bandyopadhyay, J. Fluid Mech. **163**, 439 (1986).
[4] K. Fukuda, A. Inouye, Y. Kawabe, and A. Hirai, J. Phys. Soc. Jpn. **54**, 4555 (1985).
[5] K. Kose, J. Phys. D **23**, 981 (1990).
[6] P. Mansfield, J. Phys. C **10**, L55 (1977).
[7] P. Mansfield and I. L. Pykett, J. Magn. Reson. **29**, 355 (1978).
[8] R. R. Rzedzian and I. L. Pykett, Am. J. Roentgenol. **149**, 245 (1987).
[9] D. N. Firmin, R. H. Klipstein, G. L. Hounsfield, M. P. Paley, and D. B. Longmore, Magn. Reson. Med. **12**, 316 (1989).
[10] K. Kose, J. Magn. Reson. **92**, 631 (1991).
[11] K. Satoh, K. Kose, T. Inouye, and H. Yasuoka, J. Appl. Phys. **57**, 2174 (1985).
[12] J. R. Singer and L. E. Crooks, Science **221**, 654 (1983).
[13] K. Kose, K. Satoh, T. Inouye, and H. Yasuoka, J. Phys. Soc. Jpn. **54**, 81 (1985).
[14] F. W. Wehrli, A. Shimakawa, J. R. MacFall, L. Axel, and W. Perman, J. Comput. Assist. Tomogr. **9**, 537 (1985).
[15] P. R. Moran, Magn. Reson. Imaging **1**, 197 (1982).
[16] D. J. Bryant, J. A. Payne, D. N. Firmin, and D. B. Longmore, J. Comput. Assist. Tomogr. **8**, 588 (1984).
[17] P. van Dijk, J. Comput Assist. Tomogr. **8**, 429 (1984).
[18] V. J. Wedeen, B. R. Rosen, D. Chesler, and T. J. Brady, J. Comput. Assist. Tomogr. **9**, 530 (1985).
[19] M. O'Donnell, Med. Phys. **12**, 59 (1985).
[20] K. Kose, T. Inouye, K. Satoh, K. Okamoto, and A. Ito, *Book of Abstracts* (Society of Magnetic Resonance in Medicine, Berkeley, CA, 1986), p. 135.
[21] V. J. Wedeen, R. E. Wendt III, and M. Jerosch-Herold, Magn. Reson. Med. **11**, 114 (1989).

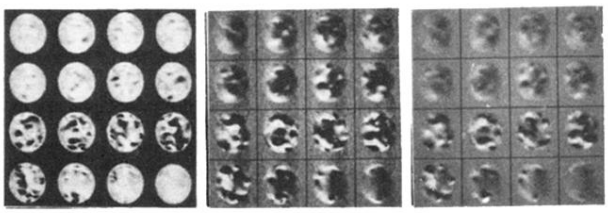

FIG. 10. (a) Real, (b) imaginary, and (c) phase images of an equilibrium puff visualized with the flow perpendicular to the pipe axis. These images are taken consecutively at 200-ms time intervals and displayed from the upper left to the lower right. The phase image directly shows distribution of the velocity component v.

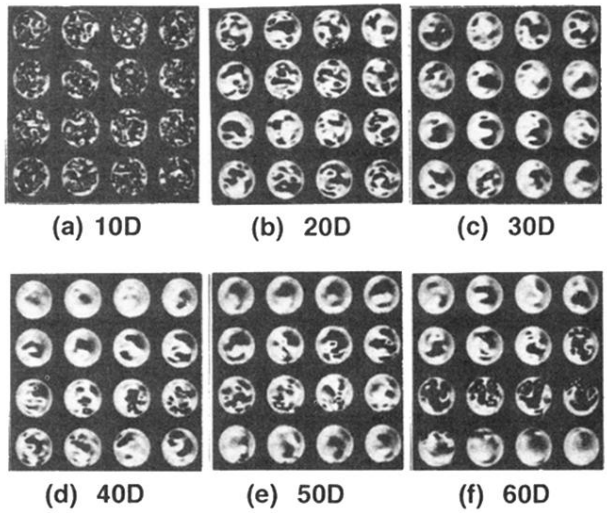

FIG. 13. Images taken at (a) $x = 10D$, (b) $20D$, (c) $30D$, (d) $40D$, (e) $50D$, and (f) $60D$. Real part images taken at 200-msec time intervals are displayed from the upper left to the lower right. These images show that the turbulence produced near the orifice gradually decay as the flow goes downstream ($x = 10D - 30D$), however, inhomogeneous turbulent distributions along the flow direction are observed at more downstream positions ($x = 40D - 60D$).

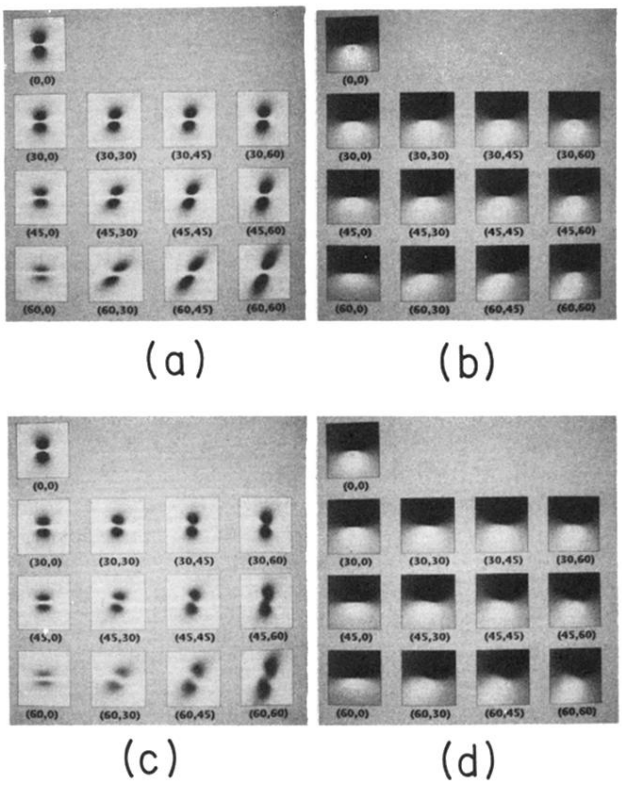

FIG. 3. Calculated images of the model vortex. The pair of numbers displayed below the images are the angles (θ,φ). (a) and (c) are real part images and (b) and (d) are imaginary part images. Slice thickness is zero in (a) and (b) and about twice as large as the diameter of the vortex core in (c) and (d).

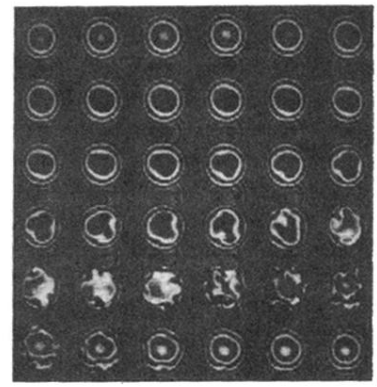

(a)

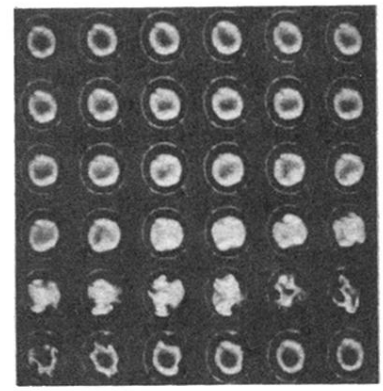

(b)

FIG. 5. Cross-sectional NMR images of equilibrium puffs visualized with the flow parallel to the pipe axis. Reynolds number is 2250. The coefficient α is 1.0 and 0.5 rad/(cm/s) in (a) and (b), respectively. 36 consecutive images taken at 200-ms time intervals are displayed from the upper left to the lower right. Only real part images are displayed.

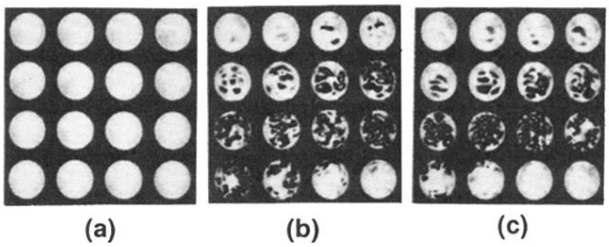

FIG. 8. Cross-sectional NMR images visualized with the flow perpendicular to the pipe axis. (a) Reynolds number is 2000. The flow is laminar and there is no flow component perpendicular to the pipe axis. (b) and (c) Reynolds number is 2250. An equilibrium puff is visualized with the flow component perpendicular to the pipe axis. 16 consecutive images are displayed from the upper left to the lower right. Only real part images are displayed.

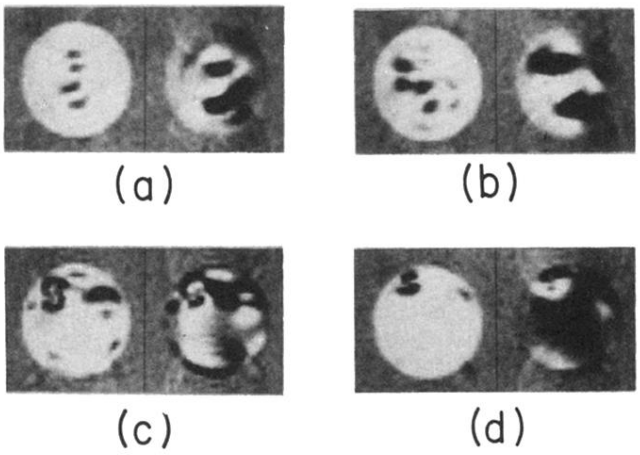

FIG. 9. Longitudinal vortices observed in the downstream region [(a) and (b)] and at the upstream interface [(c) and (d)]. The left and right images show real and imaginary images, respectively. (c) and (d) are consecutive images taken in an equilibrium puff.